Deep Entry of Low-Energy Ions Into Mercury's Magnetosphere: BepiColombo Mio's Third Flyby Observations

Yuki Harada, Yoshifumi Saito, Lina Hadid, Dominique Delcourt, Sae Aizawa, Mathias Rojo, Nicolas André, Moa Persson, Markus Fraenz, Shoichiro Yokota, et al.

JGR Space Physics

RESEARCH ARTICLE
10.1029/2024JA032751

Deep Entry of Low-Energy Ions Into Mercury's Magnetosphere: BepiColombo Mio's Third Flyby Observations

Yuki Harada[1], Yoshifumi Saito[2], Lina Z. Hadid[3], Dominique Delcourt[3], Sae Aizawa[3], Mathias Rojo[4], Nicolas André[4,5], Moa Persson[6], Markus Fraenz[7], Shoichiro Yokota[8], Andréi Fedorov[4], Wataru Miyake[9], Emmanuel Penou[4], Alain Barthe[4], Jean-André Sauvaud[4], Bruno Katra[3], Shoya Matsuda[10], and Go Murakami[2]

[1]Department of Geophysics, Graduate School of Science, Kyoto University, Kyoto, Japan, [2]Institute of Space and Astronautical Science, Japan Aerospace Exploration Agency, Tokyo, Japan, [3]Laboratoire de Physique des Plasmas (LPP), CNRS, Observatoire de Paris, Sorbonne Université, Université Paris Saclay, Ecole Polytechnique, Institut Polytechnique de Paris, Palaiseau, France, [4]IRAP, CNRS-UPS-CNES, Toulouse, France, [5]Institut Supérieur de l'Aéronautique et de l'Espace (ISAE-SUPAERO), Université de Toulouse, Toulouse, France, [6]Swedish Institute of Space Physics, Uppsala, Sweden, [7]Max-Planck-Institute for Solar System Research, Göttingen, Germany, [8]Department of Earth and Space Science, Graduate School of Science, Osaka University, Osaka, Japan, [9]Tokai University, Kanagawa, Japan, [10]Graduate School of Natural Science and Technology, Kanazawa University, Kanazawa, Japan

Key Points:

- BepiColombo Mio observed low-energy dense ions deep within Mercury's magnetosphere during the third Mercury flyby
- Backward test particle simulations suggest that low-energy ions are transported by convection from the duskside tail magnetopause
- Forward test particle simulations imply convection-driven ion precipitation onto the nightside low-latitude surface of Mercury

Correspondence to:
Y. Harada,
haraday@kugi.kyoto-u.ac.jp

Citation:
Harada, Y., Saito, Y., Hadid, L. Z., Delcourt, D., Aizawa, S., Rojo, M., et al. (2024). Deep entry of low-energy ions into Mercury's magnetosphere: BepiColombo Mio's third flyby observations. *Journal of Geophysical Research: Space Physics*, *129*, e2024JA032751. https://doi.org/10.1029/2024JA032751

Received 14 APR 2024
Accepted 26 JUL 2024

Abstract Although solar wind-driven convection is expected to dominate magnetospheric circulation at Mercury, its exact pattern remains poorly characterized by observations. Here we present BepiColombo Mio observations during the third Mercury flyby indicative of convection-driven transport of low-energy dense ions into the deep magnetosphere. During the flyby, Mio observed an energy-dispersed ion population from the duskside magnetopause to the deep region of the midnight magnetosphere. A comparison of the observations with backward test particle simulations suggests that the observed energy dispersion structure can be explained in terms of energy-selective transport by convection from the duskside tail magnetopause. We also discuss the properties and origins of more energetic ions observed in the more dipole-like field regions of the magnetosphere in comparison to previously reported populations of the plasma sheet horn and ring current ions. Additionally, forward test particle simulations predict that most of the observed ions on the nightside will precipitate onto relatively low-latitude regions of the nightside surface of Mercury for a typical convection case. The presented observations and simulation results reveal the critical role of magnetospheric convection in determining the structure of Mercury's magnetospheric plasma. The upstream driver dependence of magnetospheric convection and its effects on other magnetospheric processes and plasma-surface interactions should be further investigated by in-orbit BepiColombo observations.

1. Introduction

Mercury has a relatively weak intrinsic magnetic field represented by a dipole moment of 190 nT-R_M^3 with a northward offset of 0.196 R_M (Anderson et al., 2012), where R_M is Mercury's radius ($R_M = 2440$ km). The solar wind interaction with Mercury's magnetic field forms a highly dynamic, small-scale magnetosphere (Slavin, 2004; Sun, Dewey, et al., 2022). Mercury's magnetosphere is unique among the solar-system magnetospheres in terms of magnetospheric circulation. In the Earth's magnetosphere, both corotation and solar wind-driven convection contribute to the global magnetospheric circulation, while the magnetospheric circulation of Jupiter and Saturn is primarily driven by corotation (e.g., Bagenal, 1992). Meanwhile, the plasma circulation inside Mercury's magnetosphere is expected to be completely dominated by solar wind-driven convection owing to the slow rotation rate of the planet (e.g., see Figure 6 of Slavin et al. (2007)). In this sense, Mercury's magnetosphere represents arguably the most strongly solar wind-driven magnetosphere in our solar system.

Plasma sources of Mercury's magnetosphere are classified into solar wind and planetary origins (Raines et al., 2015; Seki et al., 2015). Proposed processes of the solar wind entry into Mercury's magnetosphere are in many ways analogous to those operating in the Earth's magnetosphere, including high-latitude entry driven by dayside magnetopause reconnection leading to the formation of the plasma mantle (DiBraccio et al., 2013, 2015; Jasinski et al., 2017) and low-latitude entry across the boundary layers by the Kelvin–Helmholtz instability

(Aizawa et al., 2020; Boardsen et al., 2010; Gershman et al., 2015; Korth et al., 2014; Liljeblad et al., 2014; Slavin et al., 2008; Sundberg et al., 2010, 2011, 2012). Planetary plasma sources include the ionization of exospheric neutral particles and the direct emission of charged particles from the planetary surface (Raines et al., 2014; Sun, Slavin, et al., 2022; Winslow et al., 2020; Zurbuchen et al., 2008, 2011). In Mercury's magnetosphere, protons of solar wind origin typically dominate over planetary heavy ions in terms of number densities while heavy ions can provide a significant contribution to pressures (Gershman et al., 2014; Raines et al., 2013; Zurbuchen et al., 2011).

One can expect that the transport of low-energy ions of both solar wind and planetary origins within Mercury's magnetosphere is strongly controlled by solar wind-driven magnetospheric convection as hinted by a comparison between MESSENGER Fast Imaging Plasma Spectrometer (FIPS) observations and a global magnetohydrodynamic simulation (Zhong et al., 2024). Despite its expected importance, the magnetospheric convection at Mercury has been poorly investigated partly because of the difficulty of deriving cold plasma velocities from currently available measurements. In this paper, we report on low-energy ion observations by BepiColombo Mio during the third Mercury flyby. Although the charged particle measurements by Mio are not yet at their full capacity due to the limited field of views during the cruise configuration (Harada et al., 2022; Murakami et al., 2020), the third flyby observations captured interesting signatures of magnetospheric ions. Specifically, the ion measurements indicate the significant presence of low-energy (<∼100 eV/q) dense ions from the duskside magnetopause deep into pre-midnight region of Mercury's magnetosphere along with more energetic populations around the midnight and dawnside regions. We conduct test particle simulations to gain deeper insights into the origins and fate of the observed ion populations. Based on the combination of the observations and simulations, we discuss the roles of magnetospheric convection at Mercury.

2. Observations

2.1. Overview

Figure 1 shows an overview of BepiColombo Mio observations of low-energy ions and electrons along with the spacecraft trajectory during the third Mercury flyby on 19 June 2023. We use the aberrated Mercury Solar Magnetospheric (MSM) coordinate system which accounts for the northward dipole offset and solar wind aberration (Harada et al., 2022; Korth et al., 2015). During this flyby, BepiColombo entered Mercury's magnetotail from the duskside magnetopause, passed by the post-midnight magnetosphere around the closest approach, and exited the magnetosphere from the dawnside magnetopause (Figures 1h–1k). Figure 1i illustrates the nightside flyby geometry in the cylindrical coordinates (Zhao et al., 2022) in comparison to the KT17 model field lines on the meridian plane (Korth et al., 2017). A notable aspect of this flyby is that the closest approach is located in the dipole-like field region in the northern hemisphere as opposed to the southern closest approaches magnetically connected to more tail-like field regions during the past two flybys (e.g., Aizawa et al., 2023; Harada et al., 2022; Orsini et al., 2022; Rojo et al., 2024).

The energy-time spectrogram of low-energy electrons obtained by one of the Mercury Electron Analyzers (MEA) (Saito et al., 2021) is shown in Figure 1a. We observe distinct changes in the electron energy spectra as indicated by the vertical gray lines corresponding to crossings of relevant boundaries. The vertical solid lines indicate the magnetopause crossings which separate the warmer magnetospheric populations and cooler magnetosheath populations. The vertical dotted line denotes the optical shadow region. The entry into the shadow coincides with the sudden decrease in electron flux. Based on the locations of the magnetopause crossings, we can infer that Mercury's magnetosphere is highly compressed during this flyby (Rojo et al., 2024). To account for the compressed state of the magnetosphere, we assume a disturbance index of 100 for the KT17 model. The other input parameter of the KT17 model, heliocentric distance, is taken from the instantaneous heliocentric distance at the flyby.

Figures 1b–1d show the energy-time spectrograms of low-energy ions obtained by the Mercury Ion Analyzer (MIA). During the third flyby of Mercury's magnetosphere, MIA operated in the solar wind mode, which uses multiple energy sweep tables (Saito et al., 2021). We utilize this data product to derive the ion energy spectra with 32 effective energy steps for each of the three energy ranges (low: ∼14–300 eV/q in Figure 1d, medium: ∼100–10 keV/q in Figure 1c, and high: ∼3–26 keV/q in Figure 1b) in time cadences of 4–16 s except for the data gaps shown in white. We observe that the ion energy spectra are distinctly different before and after the magnetopause crossings (indicated by the vertical solid lines in Figures 1b–1d) and the timings of the spectral changes are consistent with the electron measurements (Figure 1a). We note that MIA measured a relatively low flux of

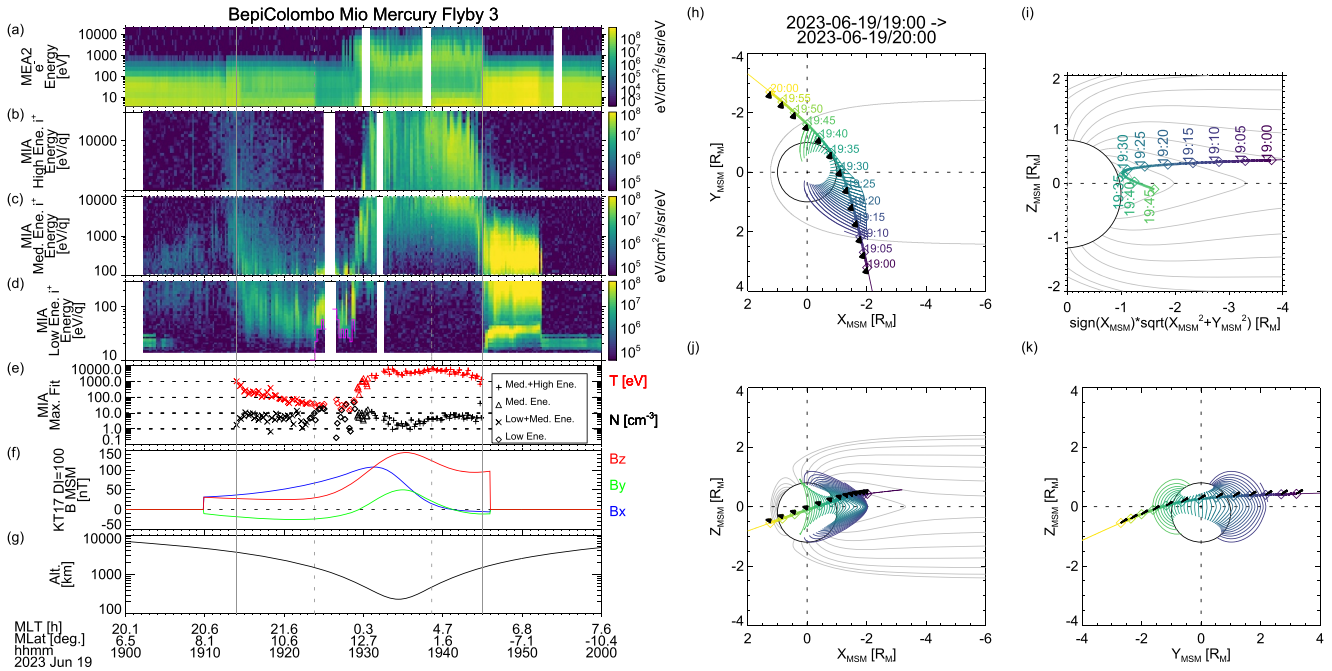

Figure 1. Overview of BepiColombo Mio observations of low-energy ions and electrons during the third Mercury flyby. Time-series of (a) electron energy spectra, (b–d) ion energy spectra in three energy ranges (high, medium, and low), (e) ion density and temperature derived from Maxwellian fitting (see text for details), (f) KT17 model magnetic field (Korth et al., 2017), and (g) spacecraft altitude. The magenta lines in panel (d) indicate the low-energy cutoff extracted from the observed ion energy spectra (see text for further details). Flyby geometry (h) projected on X_{MSM}-Y_{MSM} plane, (i) in $(\mathrm{sign}(X_{MSM})\sqrt{X_{MSM}^2 + Y_{MSM}^2})$-$Z_{MSM}$ coordinates highlighting the spacecraft trajectory in the tail field configuration, and projected on the (j) X_{MSM}-Z_{MSM} and Y_{MSM}-Z_{MSM} planes. The colored curves in panels (h, j, k) indicate the magnetic field lines traced from the BepiColombo locations in the KT17 model. The black fans in panels (h, j, k) denote MIA's effective field of view in the cruise-phase configuration. The gray curves in panels (i, j) show the KT17 model magnetic field lines on the noon-midnight meridian for reference. The instantaneous heliocentric distance and a disturbance index of 100 are used as input parameters for the KT17 model.

magnetosheath ions in the inbound segment while the intense flux was observed in the outbound magnetosheath. This inbound-outbound difference in the magnetosheath, also observed during the first Mercury flyby, likely arises from the limited field of view (FOV) of MIA due to the sunshield blockage in the cruise phase configuration (Harada et al., 2022; Murakami et al., 2020). In the inbound magnetosheath, MIA's FOV was nearly perpendicular to the expected magnetosheath flow diverging along the magnetopause as shown in Figure 1h. This configuration suggests a large portion of the ion velocity distribution was unmeasurable by MIA. Meanwhile, MIA's FOV was more favorable in detecting the magnetosheath ions flowing dawnward and tailward in the dawnside outbound magnetosheath. The limited FOV prevents MIA from directly measuring the upstream solar wind. We also note that the strong fluxes of cold ions with narrowband features at <~50 eV/q outside the magnetopause (before 19:06 UTC and after 19:45 UTC in Figure 1d) presumably arise from spacecraft outgassing (Fränz et al., 2024) and should not be considered as ambient ions.

Within the magnetopause, MIA measured a wide energy range of magnetospheric ions as low as ~20 eV/q up to the highest measured energy of ~20 keV/q with different energy spectra observed in different regions (Figures 1b–1d). Note that the magnetic local time (MLT) and magnetic latitude (MLat) (see Equations 1a–1c of Anderson et al. (2013) for definition) are indicated along the time axis. Based on the energy-time structures, we categorize the magnetospheric ions into three populations: (a) duskside ions gradually changing their energy characteristics from broad energies just within the magnetopause to low energies (<~300 eV/q) just before the midnight region (observed during 19:13–19:29 UTC); (b) ~1 keV/q ions observed around the midnight region (19:29–19:31 UTC) representing a transition from the low to high energy populations; and (c) energetic ~10 keV ions observed in the dipole-like field region on the dawnside (19:31–19:45 UTC). Ion composition measurements by the Mass Spectrum Analyzer (MSA) indicate that protons are the dominant species for these ion populations, suggesting their solar wind origin, although minor components of heavy ions are also observed. The ion energy-mass spectra are analyzed in detail in a separate paper.

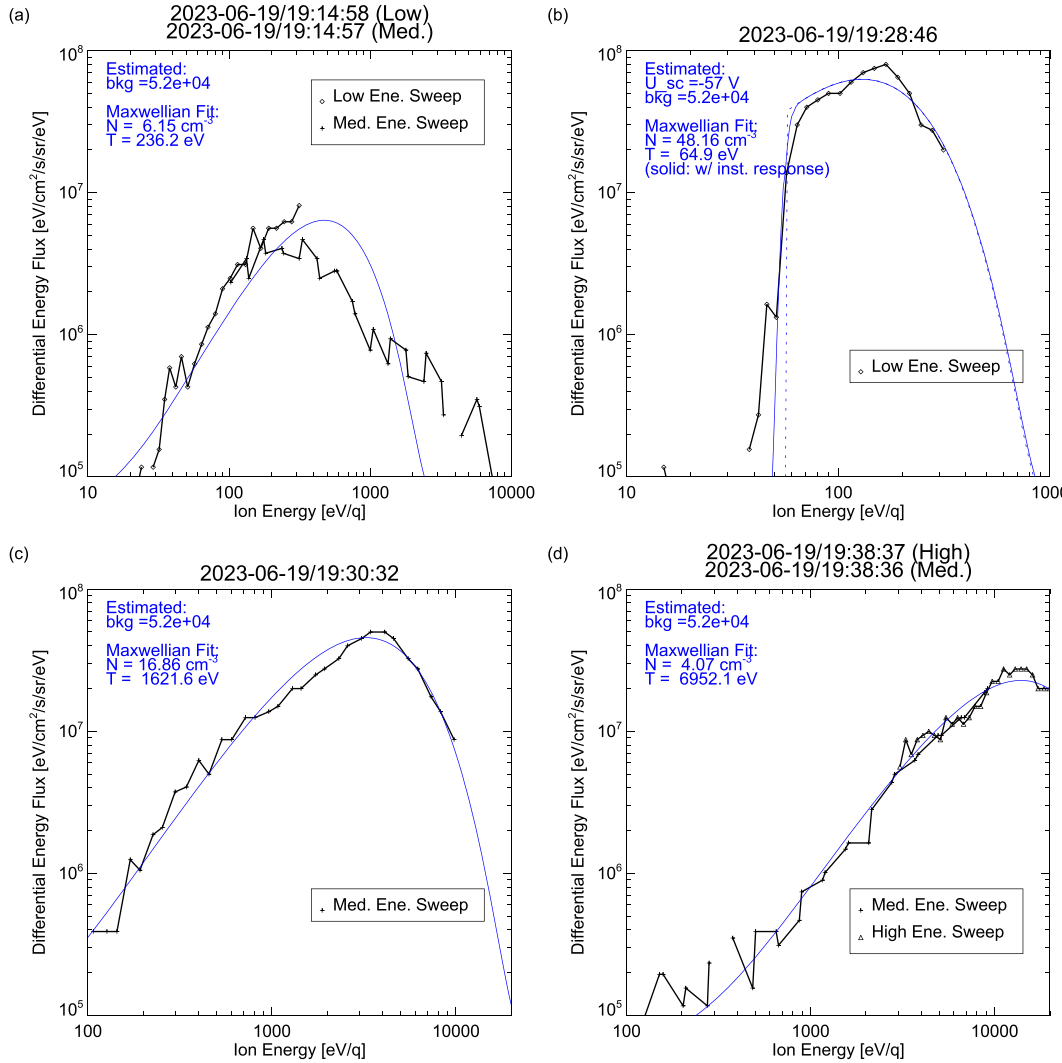

Figure 2. Examples of measured ion energy spectra and Maxwellian fitting results at (a) 19:14:57–58 UTC, (b) 19:28:46 UTC, (c) 19:30:32 UTC, and (d) 19:38:36–37 UTC. In panel (b), the dotted curve shows the Maxwellian energy spectrum shifted according to the estimated negative spacecraft potential such that the distribution function is conserved, and the solid curve shows the predicted measurement derived from convolution with MIA's energy response. In panels (a, c, and d), the spacecraft potential is assumed to be zero.

To further characterize the observed magnetospheric ion populations, we derive the ion density and temperature parameters from Maxwellian fits to the observed 1D ion energy spectra under the isotropic and proton-only assumptions (Figures 1e and 2). Since these assumptions could become inadequate depending on the ion velocity distributions (full information on which cannot be measured by Mio in the cruise configuration due to the limited field of views of particle instruments), the derived parameters are likely to include large uncertainties and should be taken as approximate estimates at best. Nevertheless, the different characteristics of the ion populations are well represented by the derived density and temperature parameters as described in the following subsections.

2.2. Duskside Energy-Dispersed Ions

We first examine the duskside ion population. Figure 2a shows the observed (black) and fitted (blue) energy spectra obtained at 19:14:57–58 UTC in the duskside magnetotail region. Around this time, the ions are measured mainly in the low and medium energy ranges (Figures 1d and 1c, respectively), and we combine these energy ranges to conduct the fitting (the results are shown by the "X" symbols in Figure 1e). Also, the fitting procedure

takes into account the background count level estimated from the high-energy range data during 19:55–20:00 UTC (during which essentially no ion signals are detected (Figure 1b)).

Figure 2b shows another example obtained at 19:28:46 UTC in the optical shadow region. In the measured spectrum, we observe a sharp cutoff at ∼60 eV/q. Similar cutoff features appear immediately after entering the optical shadow (Figure 1d). This low-energy cutoff in shadow is presumably caused by negative spacecraft charging, which accelerates the ambient ions before being detected by the instrument (e.g., Seki et al., 2003). We identify the low-energy cutoff based on an empirically determined threshold of a flux drop level (1/20 of the peak flux or 4×10^5 eV/cm^2/s/sr/eV whichever is higher) for the low-energy ion populations measured in the optical shadow. The identified cutoff energies are shown by the magenta lines in Figure 1d, which successfully track the measured cutoff features. Based on the identified cutoff energy, we can estimate the negative spacecraft potential. The negative spacecraft potential seems to be highly variable (Figure 1d) possibly because of the varying electron temperature (Figure 1a, see also Rojo et al., 2024), which is the main driver of the negative charging. We take into account the estimated negative spacecraft potential as well as MIA's energy response (approximated by a Gaussian with a full width at half maximum of 12.7% (Saito et al., 2021)) in our fitting procedure as demonstrated in Figure 2b. For measurements in sunlight, we assume a zero spacecraft potential, which potentially results in an underestimation of the ion density if the actual spacecraft potential is positive. The fitting results for the low-energy range spectra are shown by the diamond symbols in Figure 1e.

The derived ion density and temperature parameters show the characteristic properties of the duskside ion population. The average energy (represented by the temperature) decreases with increasing distance from hundreds of eV near the magnetopause down to tens of eV in the shadow region (see the red "X" and diamond symbols in Figure 1e). This is in line with the energy dispersion structure seen in the energy-time spectrograms, namely the decreasing trends in the overall and higher-end energies of this ion population (Figures 1b–1d). Another remarkable property is that the ion density reaches as high as tens of cm^{-3} in the optical shadow during 19:24–19:29 UTC even though this population is observed in the very deep region of the magnetosphere (Figures 1h and 1i). The estimated densities are roughly an order of magnitude higher than the average proton density in the corresponding region reported from MESSENGER FIPS measurements (Zhao et al., 2020), implying the presence of a relatively dense low-energy ion population in the deep magnetosphere that is perhaps not well characterized by the FIPS measurements that are limited to >50 eV/q (Andrews et al., 2007).

2.3. Midnight ~1 keV Ions

In this subsection, we briefly present the properties of the midnight ∼1 keV ions. Figure 2c shows an ion energy spectrum obtained at 19:30:32 UTC just around MLT ∼0 as labeled along the time axis in Figure 1. Around this time, the main ion population is measured in the medium energy range (Figure 1c), and the Maxwellian fit parameters to this energy range are shown by the triangles in Figure 1e. The derived ion density and temperature are around 10 cm^{-3} and 1 keV, respectively.

2.4. Dawnside ~10 keV Ions

We now investigate the properties of the ∼10 keV ions observed on the dawnside magnetosphere. Figure 2d shows an ion energy spectrum obtained at 19:38:36–37 UTC. We can see that the peak and low-energy side of the observed spectrum is well represented by a Maxwellian, though the high-energy side of this population exceeds MIA's energy range. We use the medium and high energy ranges for the Maxwellian fitting to this ion population (Figures 1b and 1c), and the fit parameters are indicated by the plus symbols in Figure 1e. The estimated density and temperature are on the order of several cm^{-3} and several keV, respectively. This energetic ion population is continuously observed from the closest approach to the dawnside magnetopause (Figures 1b and 1c), where the field line configuration is expected to be more or less dipole-like (Figures 1h–1k). Approaching the dawnside magnetopause, we observe the decrease and fluctuation of the upper edge energy of the detected ion population during 19:41–19:45 UTC (Figure 1b). The observed energies and locations are generally consistent with ring current ions first identified by MESSENGER FIPS (Zhao et al., 2022). The energetic ion population in the inner magnetosphere is also reminiscent of the plasma belt mentioned in Shi et al. (2022).

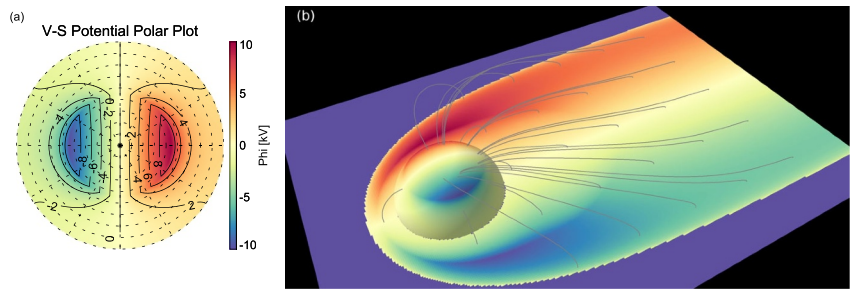

Figure 3. Volland-Stern electric potential distributions for a potential drop of 20 kV without corotation used in the test particle simulations (a) in the MLT-MLat polar map (pole = center, equator = outermost circle, noon = up, midnight = down) and (b) in a 3-dimensional plot depicting magnetic field line mapping (gray lines) from the *X*-*Y* plane at $Z = 0$ to the $0.8R_M$ reference sphere. An electric potential at a given position in the magnetosphere is derived from the corresponding potential on the $0.8R_M$ reference sphere assuming equipotential along the magnetic field lines.

3. Test Particle Simulations

3.1. Simulation Setup

To help interpret the MIA observations during the third Mercury flyby, we conduct simple test particle simulations. We trace protons in static magnetic and electric fields from the observed locations both backward and forward in time, thereby inferring the origins and fate of the observed ions. In this subsection, we describe the simulation setup.

For the background magnetic field, we use the KT17 model with the aforementioned choice of a disturbance index of 100 to approximate the global magnetic field configuration of the compressed magnetosphere during the third Mercury flyby. We also conduct additional simulations with other choices of the disturbance index (0 for an expanded magnetosphere and 50 for a nominal-size magnetosphere), the results of which are discussed as needed in the following subsections.

For the background electric field, we utilize the Volland-Stern potential description without corotation to express the large-scale magnetospheric convection (Delcourt et al., 2011; Volland, 1978) as shown in Figure 3. The electric potential is given by

$$\phi = \begin{cases} \phi_{PC} \dfrac{\sin\theta}{\sin\theta_{CRB}} \sin\tau & (\theta < \theta_{CRB}) \\ \phi_{PC} \dfrac{\sin^4\theta_{CRB}}{\sin^4\theta} \sin\tau & (\theta \geq \theta_{CRB}) \end{cases}, \tag{1}$$

where τ is MLT, θ is colatitude, ϕ_{PC} is the cross-polar cap potential drop, and θ_{CRB} is the colatitude at the Convection Reversal Boundary (CRB), which is derived from the open-closed boundary on the midnight meridian according to the assumed magnetic field configuration. More detailed descriptions can be found in the Introduction of Volland (1978) and on page 988 of Delcourt et al. (2011). Figure 3a shows a polar plot of the MLT–MLat distribution of the Volland Stern potential for $\phi_{PC} = 20$ kV, representing a simple two-cell pattern. We assume $\phi_{PC} = 20$ kV as a typical potential drop according to previous estimates from plasma mantle observations (DiBraccio et al., 2015; Jasinski et al., 2017). We also conduct no convection case ($\phi_{PC} = 0$) for reference, and the results are discussed as needed in the following subsections.

Here we describe the detailed implementation of electric field calculation. For a given point in the magnetosphere, we trace the KT17 model magnetic field line to a reference sphere surface with a radius of 0.8 R_M centered at the magnetic dipole, and τ and θ of the field-line foot point are used for the Volland-Stern potential calculation according to Equation 1 assuming equipotential along the magnetic field line. We arbitrarily chose the 0.8 R_M reference sphere for a practical reason; any location above the planetary surface is outside this 0.8 R_M sphere from the dipole (cf. the northward 0.196 R_M dipole offset (Anderson et al., 2012)), and thus we can trace the field line inward to the 0.8 R_M sphere and assign the Volland-Stern potential anywhere above the planetary surface in the magnetosphere. Figure 3b demonstrates the magnetic field line mapping from the *X*–*Y* plane at $Z = 0$ to the 0.8 R_M

reference sphere and the mapped potential distribution on the X–Y plane. One can see generally dawn-to-dusk electric fields in the magnetotail as derived from the Volland-Stern potential. To efficiently track as many particles as possible, we generate a pre-calculated look-up table (LUT) of the Volland-Stern electric fields in the magnetosphere at cartesian regular grids (0.025 R_M resolution at $-4R_M < X < 2R_M$, and 0.05 R_M resolution at $-22R_M < X < -4R_M$), and an electric field at a given point is derived from trilinear interpolation of the 3-dimensional LUT. We note that the electric field used in this study is necessarily oversimplified and provides only a crude approximation of global magnetospheric convection. For example, the Volland-Stern potential cannot describe dynamic and complex electric fields that are expected to be present around the tail reconnection point and the resulting local structures such as plasmoids and tail flux ropes in the tail current sheet. Also, the assumed typical potential drop of 20 kV may not necessarily be representative of this specific event. More realistic electric fields, such as those derived from global self-consistent simulations, should be incorporated in future studies.

For a specified configuration of the magnetic and electric fields, we launch a large number of test particles from initial positions along the BepiColombo trajectory. Specifically, we set the initial positions at 36 timings during the flyby with a 1-min cadence from 19:10 to 19:45 UTC. From each of the initial positions, we launch protons with initial velocities at 16 logarithmic energy steps from 20 eV to 20 keV in 32 directions (the full sky is divided quasi-isotropically), resulting in $36 \times 16 \times 32 = 18,432$ particles launched in total per each field configuration. We trace the test particles using fourth-order Runge-Kutta integration with a time step of 1/128 of gyration or 1 km/velocity whichever is smaller. We stop tracing if the time step reaches 2^{17}, the particle strikes the planetary surface, or the particle approaches the magnetopause within 0.2 R_M. We introduced this 0.2 R_M margin according to the estimated low latitude boundary layer thickness of ~450 km ~0.18 R_M (Liljeblad et al., 2015) because the electric and magnetic fields in the boundary layers are not appropriately represented by the simple field configuration. For the backward (negative time steps) and forward (positive time steps) test particle simulations, subsets of the calculated particle trajectories and statistical representation of the final particle positions are shown in Figures 4 and 5, respectively, and the results are discussed in the following subsections.

3.2. Origins of the Observed Ions

We first investigate the duskside ion population with energy dispersion from the backward tracing results. Figures 4a1–4a3 show representative particle trajectories with the initial positions and energies indicated by the colored plus signs in Figure 4d1 and with the initial pitch angles of 100°–120° based on the approximate pitch angle coverage estimated from the KT17 model field direction and MIA's effective field of view. We can see that the observed ions are traced back to the dusk-to-midnight tail magnetopause. In this typical convection case of $\phi_{PC} = 20$ kV, the perpendicular drift of the low-energy (<~100 eV) ions is primarily driven by the convection electric field, leading to the deep entry of the low-energy ions from the tail magnetopause to the observed locations. This convection-driven transport should be more effective for lower-energy ions, and the resulting energy-dependent entry paths from the tail magnetopause could give rise to the energy dispersion structure as observed by MIA. This velocity filter effect is similar to cusp-reflected ions forming the plasma mantle with energy dispersion (DiBraccio et al., 2015; Jasinski et al., 2017; Raines et al., 2015), but here we consider ions injected from the tail magnetopause as suggested by Figures 4a1–4a3. Broad energy ions injected from the tail magnetopause travel along the magnetic field lines toward Mercury while drifting perpendicularly toward the central plasma sheet by the $\mathbf{E} \times \mathbf{B}$ drift due to the large-scale tail lobe convection. Since the $\mathbf{E} \times \mathbf{B}$ drift velocity does not depend on the particle energy, the lower-energy ions with slower parallel velocities can drift perpendicularly to the deeper region of the magnetosphere. We explore this hypothesis by comparing the test particle simulation results with the observed energy-time structure in Figure 4d1–4d3. Figures 4d2 and 4d3 show the X and Y coordinates of the final particle positions, respectively, exhibiting the locations of the inferred ion origins in the energy-time spectrogram format (here the time axis essentially represents the initial positions of the test particles along the flyby trajectory). If we assume a hypothetical ion injection region on the duskside mid-tail magnetopause at $X > -12R_M$ and $Y > 0$, then ions from this source region are predicted to be observed with the energy-time structure indicated by the magenta diamonds in Figures 4d2–4d3. The predicted energy dispersion structure is favorably compared with the observed one as shown in Figure 4d1. This suggests that the observed energy-dispersed ions on the duskside can be explained by the ion injection from the duskside tail magnetopause and subsequent energy-selective ion transport by magnetospheric convection.

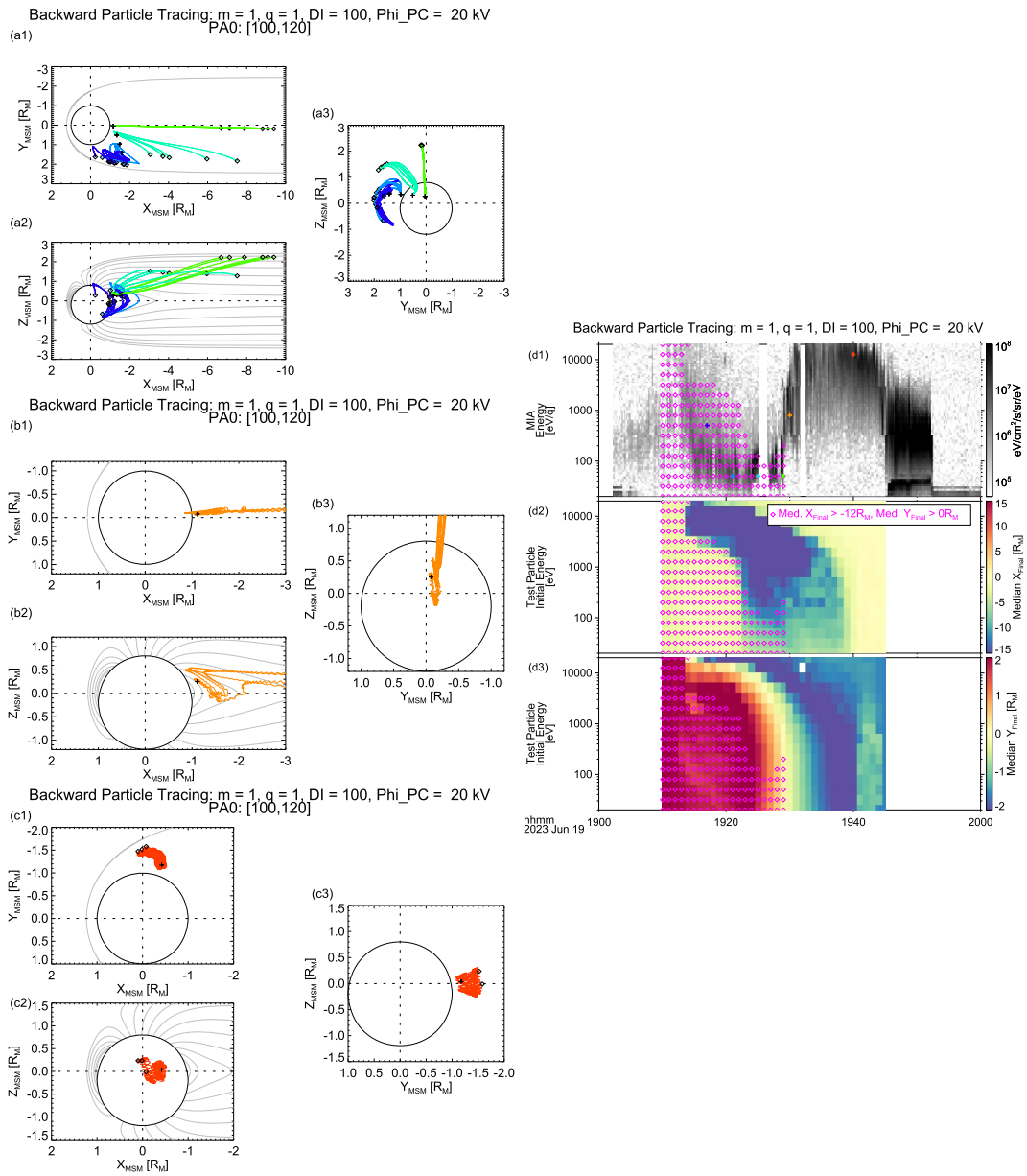

Figure 4. Representative results of backward test particle simulations. Test particle trajectories projected on the (a1, b1, c1) X_{MSM}-Y_{MSM}, (a2, b2, c2) X_{MSM}-Z_{MSM}, and (a3, b3, c3) Y_{MSM}-Z_{MSM} planes for an initial pitch angle range of 100°–120° launched at the energies and locations indicated by the colored plus symbols shown in the measured ion energy-time spectrograms (d1). In panels (a1–c3), the plus signs indicate the initial positions of backward tracing (i.e., detection by MIA), while the diamond signs show the final positions of backward tracing (estimated origins of the detected ions). The median (d2) X and (d3) Y of the final test particle positions for each initial energy-position (time) bin in comparison to (d1) the measured ion energy-time spectrogram. In panels (d1–d3), the magenta diamonds show the energy-time structure resulting from an inferred source region of $X > -12R_M$ and $Y > 0$.

We also note that for the no convection case with $\phi_{PC} = 0$, the low-energy ions continue to bounce between mirror points and magnetically drift very slowly until the maximum time step (not shown), indicating that they can stay for a long time in the deep magnetosphere in the absence of electric fields. This in turn suggests that some kind of electric fields are required to bring these ions to such a deep region of the magnetosphere in the first place. Although detailed injection processes from the magnetopause and dynamics of the plasma transport within the magnetosphere remain elusive, the test particle simulation results suggest the important role of magnetospheric

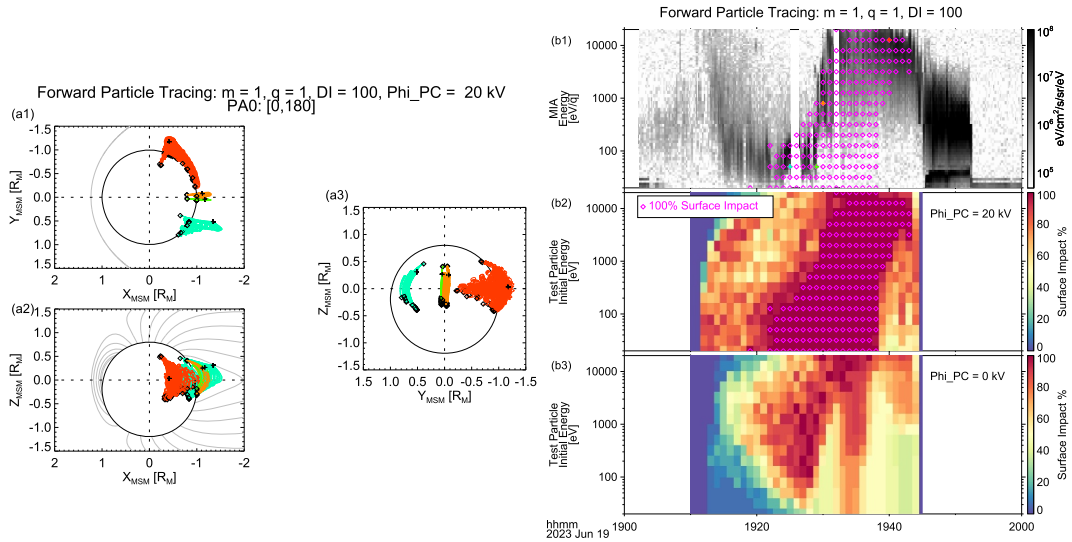

Figure 5. Representative results of forward test particle simulations. Test particle trajectories projected on the (a1) X_{MSM}-Y_{MSM}, (a2) X_{MSM}-Z_{MSM}, and (a3) Y_{MSM}-Z_{MSM} planes for the full range of initial pitch angles launched at the energies and locations indicated by the colored plus signs shown in the measured ion energy-time spectrogram (b1). In panels (a1–a3), the plus signs indicate the initial positions of forward tracing (i.e., detection by MIA), while the diamond signs show the final positions of forward tracing (estimated fate of the detected ions). Fractions of the test particles that impact the surface of Mercury in the forward tracing results for (b2) typical and (b3) zero convection cases. In panels (b1) and (b2), the magenta diamonds indicate the energy-time bins in which all particles impact the planetary surface in the typical convection case.

convection in low-energy plasma transport that enables the presence of the relatively dense, low-energy ions observed in the deep magnetosphere.

Figures 4b1–4b3 show a subset of the test particle simulation results relevant to the midnight ∼1 keV ions (indicated by the orange plus sign in Figure 4d1). As shown by the test particle trajectories in Figures 4b1–4b3, the midnight ∼1 keV ions are first traced back to the near-tail magnetic equator and then exhibit nonadiabatic chaotic motion around the cross-tail current sheet ($Z_{MSM} = 0$ at $X_{MSM} < \sim -1.5R_M$ (Korth et al., 2015)). From these results, we can infer that the immediate origin of the midnight ∼1 keV ions is the near-tail plasma sheet, but the exact locations of their ultimate origins are harder to identify. The predicted structure of the near-tail plasma sheet population extended to the higher latitudes along the magnetic field lines is a characteristic of the "plasma sheet horns," and the observed location and energy of the midnight ∼1 keV ions are consistent with the reported observations of Mercury's northern plasma sheet horn (Glass et al., 2022).

A similar exercise for the dawnside ∼10 keV ions (indicated by the red plus sign in Figure 4d1) is shown in Figures 4c1–4c3. These energetic ions are traced back to the dawnside magnetopause, suggesting a partial drift path on the dawnside although energization processes remain unclear. This partial drift path is in stark contrast to the complete drift paths of ring current ions around the planet via either the equatorial orbit or the bifurcated Shabansky orbit (Shabansky, 1971; Walsh et al., 2013) as proposed by Zhao et al. (2022) based on MESSENGER FIPS observations and test particle simulation results for low and moderate solar wind dynamic pressure cases in zero electric fields. However, we note that the interpretation of the partial or full ring current is heavily dependent on the choice of the magnetic field configuration. If we assume a more expanded state of the magnetosphere (disturbance index of 0 or 50) in both the no convection ($\phi_{PC} = 0$) and typical convection ($\phi_{PC} = 20$ kV) cases, test particle tracing suggests that some of the energetic ions follow the Shabansky orbit and continue drifting over the dayside (not shown). Future studies should address the dependence of the ion trajectories on model fields as well as ion energization processes. Without the upstream solar wind information and a direct comparison of magnetometer measurements with the model prediction, we cannot make a definitive conclusion as to whether the observed energetic ions represent partial or full ring current ions. The still unclear structure, dynamics, and energization processes of Mercury's ring current ions warrant further investigation.

3.3. Fate of the Observed Ions

We next examine the forward-in-time particle tracing results shown in Figure 5. From the representative trajectories in the compressed magnetosphere and typical convection case (Figures 5a1–5a3) of the detected ion populations (see the colored plus signs in Figure 5b1), we can see that these ions are predicted to drift inward because of the magnetospheric convection and eventually impact the relatively low-latitude regions of the nightside surface of Mercury. The predicted ion precipitation is statistically demonstrated in Figure 5b2, which shows the fraction of the launched particles impacting the planetary surface in each initial energy-position bin (note that the time axis corresponds to the initial positions along the BepiColombo flyby trajectory). The dark red color bins with magenta diamonds indicate that all of the launched particles impact the surface. We observe the energy dependence of this dark red region at 19:20–19:30 UTC because the lower-energy ions are more effectively transported by convection to the surface while the higher-energy ions can magnetically drift westward around the planet more quickly than the electric field-driven convection. Meanwhile, we see that even high-energy ions at 19:30–19:40 UTC are predicted to impact the surface (Figure 5b2) because of the gradual inward convection during the longer drift path from the dawnside over the nightside (Figure 5a1). This suggests that most of the observed ions during 19:20–19:40 UTC (indicated by the magenta diamonds in Figure 5b1) will precipitate to the nightside surface of Mercury under the typical convection condition. Meanwhile, Figure 5b3 shows the results for the no convection case in the same format as Figure 5b2. In stark contrast to the typical convection case (Figure 5b2), we do not see a prevailing dark red region in the no convection case (Figure 5b3). This demonstrates that the predicted precipitation of the observed ions is primarily driven by magnetospheric convection in the test particle simulations.

4. Conclusions and Implications

MIA measured multiple populations of magnetospheric ions in a wide energy range during the third Mercury flyby: (a) energy-dispersed ions in the dusk-to-midnight magnetotail with the low-energy (several tens of eV) ions reaching the deep midnight magnetosphere with estimated densities of tens of cm^{-3}, (b) $\sim$ keV ions with densities of $\sim$10 cm^{-3} around the midnight region, and (c) $\sim$10 keV ions with densities of several cm^{-3} in the dipolar field region. To infer the origins of these ion populations, we conduct test particle simulations by tracing protons backward in time from the observed locations in the KT17 magnetic field and Volland-Stern electric potentials without corotation. The simulation results assuming a compressed state of the magnetosphere (inferred from the observations) and a typical cross-polar cap potential drop (based on the previous observations) suggest that (a) the low-energy dense ions are likely transported by magnetospheric convection from the duskside tail magnetopause, (b) the $\sim$keV ions around midnight correspond to ions in the plasma sheet horn region, and (c) the $\sim$10 keV ions could consist of possibly partial ring current ions directly injected from the dawnside magnetopause. We also conduct test particle tracing forward in time, the results of which imply that most of the observed ions on the nightside are bound to impact the surface of Mercury due to magnetospheric convection under a typical cross-polar cap potential drop. This convection-driven ion precipitation onto the low-latitude nightside surface of Mercury is characterized by a wider variety of energy spectra in comparison to the cusp precipitation (Raines et al., 2014, 2022; Winslow et al., 2014) and plasma sheet horn precipitation (Glass et al., 2022), and could lead to different consequences in plasma-surface interactions. The significance of the convection-driven ion precipitation at Mercury should depend on the nature and intensity of magnetospheric convection and on the plasma injection processes at the magnetopause, all of which are not yet fully understood. Taken together, the presented BepiColombo Mio observations and test particle simulation results reinforce the idea that magnetospheric convection plays a critical role in controlling the structure and dynamics of Mercury's magnetospheric plasma. In-orbit observations by BepiColombo Mio and Mercury Planetary Orbiter will help elucidate the plasma entry and transport into Mercury's magnetosphere as well as their dependence on upstream drivers and impacts on magnetospheric dynamics and plasma-surface interactions at Mercury.

Data Availability Statement

The MIA and MEA data used in this paper are archived and publicly available (Harada et al., 2024).

Acknowledgments
YH acknowledges support through JSPS KAKENHI Grant (22K14085, 22H01285, 22KK0045). M.R. was funded by a CNES postdoctoral fellowship and is now funded by the European Union's Horizon 2020 program under grant agreement No 871149 for Europlanet 2024 RI. French co-authors acknowledge the support of CNES for the BepiColombo mission.

References

Aizawa, S., Harada, Y., André, N., Saito, Y., Barabash, S., Delcourt, D., et al. (2023). Direct evidence of substorm-related impulsive injections of electrons at mercury. *Nature Communications*, *14*(1), 4019. https://doi.org/10.1038/s41467-023-39565-4

Aizawa, S., Raines, J. M., Delcourt, D., Terada, N., & André, N. (2020). Messenger observations of planetary ion characteristics in the vicinity of kelvin-Helmholtz vortices at mercury. *Journal of Geophysical Research: Space Physics*, *125*(10), e2020JA027871. https://doi.org/10.1029/2020JA027871

Anderson, B. J., Johnson, C. L., & Korth, H. (2013). A magnetic disturbance index for Mercury's magnetic field derived from MESSENGER Magnetometer data. *Geochemistry, Geophysics, Geosystems*, *14*(9), 3875–3886. https://doi.org/10.1002/ggge.20242

Anderson, B. J., Johnson, C. L., Korth, H., Winslow, R. M., Borovsky, J. E., Purucker, M. E., et al. (2012). Low-degree structure in Mercury's planetary magnetic field. *Journal of Geophysical Research*, *117*(E12), E00L12. https://doi.org/10.1029/2012JE004159

Andrews, G. B., Zurbuchen, T. H., Mauk, B. H., Malcom, H., Fisk, L. A., Gloeckler, G., et al. (2007). The energetic particle and plasma spectrometer instrument on the messenger spacecraft. *Space Science Reviews*, *131*(1), 523–556. https://doi.org/10.1007/s11214-007-9272-5

Bagenal, F. (1992). Giant planet magnetospheres. *Annual Review of Earth and Planetary Sciences*, *20*(1), 289–328. https://doi.org/10.1146/annurev.ea.20.050192.001445

Boardsen, S. A., Sundberg, T., Slavin, J. A., Anderson, B. J., Korth, H., Solomon, S. C., & Blomberg, L. G. (2010). Observations of Kelvin-Helmholtz waves along the dusk-side boundary of Mercury's magnetosphere during MESSENGER's third flyby. *Geophysical Research Letters*, *37*(12), L12101. https://doi.org/10.1029/2010GL043606

Delcourt, D. C., Moore, T. E., & Fok, M.-C. H. (2011). On the effect of IMF turning on ion dynamics at Mercury. *Annals of Geophysics*, *29*(6), 987–996. https://doi.org/10.5194/angeo-29-987-2011

DiBraccio, G. A., Slavin, J. A., Boardsen, S. A., Anderson, B. J., Korth, H., Zurbuchen, T. H., et al. (2013). MESSENGER observations of magnetopause structure and dynamics at Mercury. *Journal of Geophysical Research*, *118*(3), 997–1008. https://doi.org/10.1002/jgra.50123

DiBraccio, G. A., Slavin, J. A., Raines, J. M., Gershman, D. J., Tracy, P. J., Boardsen, S. A., et al. (2015). First observations of Mercury's plasma mantle by MESSENGER. *Geophysical Research Letters*, *42*(22), 9666–9675. https://doi.org/10.1002/2015GL065805

Fränz, M., Rojo, M., Cornet, T., Hadid, L. Z., Saito, Y., André, N., et al. (2024). Spacecraft outgassing observed by the bepicolombo ion spectrometers. *Journal of Geophysical Research: Space Physics*, *129*(1), e2023JA032044. https://doi.org/10.1029/2023JA032044

Gershman, D. J., Raines, J. M., Slavin, J. A., Zurbuchen, T. H., Sundberg, T., Boardsen, S. A., et al. (2015). Messenger observations of multiscale kelvin-Helmholtz vortices at mercury. *Journal of Geophysical Research: Space Physics*, *120*(6), 4354–4368. https://doi.org/10.1002/2014JA020903

Gershman, D. J., Slavin, J. A., Raines, J. M., Zurbuchen, T. H., Anderson, B. J., Korth, H., et al. (2014). Ion kinetic properties in mercury's pre-midnight plasma sheet. *Geophysical Research Letters*, *41*(16), 5740–5747. https://doi.org/10.1002/2014GL060468

Glass, A. N., Raines, J. M., Jia, X., Sun, W., Imber, S., Dewey, R. M., & Slavin, J. A. (2022). Observations of mercury's plasma sheet horn: Characterization and contribution to proton precipitation. *Journal of Geophysical Research: Space Physics*, *127*(12), e2022JA030969. https://doi.org/10.1029/2022JA030969

Harada, Y., Aizawa, S., Saito, Y., André, N., Persson, M., Delcourt, D., et al. (2022). Bepicolombo Mio observations of low-energy ions during the first mercury flyby: Initial results. *Geophysical Research Letters*, *49*(17), e2022GL100279. https://doi.org/10.1029/2022GL100279

Harada, Y., Saito, Y., Hadid, L., Delcourt, D., Aizawa, S., Rojo, M., et al. (2024). BepiColombo Mio MIA and MEA2 data during the third mercury flyby [Dataset]. *Zenodo*. https://doi.org/10.5281/zenodo.10971780

Jasinski, J. M., Slavin, J. A., Raines, J. M., & DiBraccio, G. A. (2017). Mercury's solar wind interaction as characterized by magnetospheric plasma mantle observations with messenger. *Journal of Geophysical Research: Space Physics*, *122*(12), 12153–12169. https://doi.org/10.1002/2017JA024594

Korth, H., Anderson, B. J., Gershman, D. J., Raines, J. M., Slavin, J. A., Zurbuchen, T. H., et al. (2014). Plasma distribution in mercury's magnetosphere derived from messenger magnetometer and fast imaging plasma spectrometer observations. *Journal of Geophysical Research: Space Physics*, *119*(4), 2917–2932. https://doi.org/10.1002/2013JA019567

Korth, H., Johnson, C. L., Philpott, L., Tsyganenko, N. A., & Anderson, B. J. (2017). A dynamic model of mercury's magnetospheric magnetic field. *Geophysical Research Letters*, *44*(20), 10147–10154. https://doi.org/10.1002/2017GL074699

Korth, H., Tsyganenko, N. A., Johnson, C. L., Philpott, L. C., Anderson, B. J., Al Asad, M. M., et al. (2015). Modular model for Mercury's magnetospheric magnetic field confined within the average observed magnetopause. *Journal of Geophysical Research*, *120*(6), 4503–4518. https://doi.org/10.1002/2015JA021022

Liljeblad, E., Karlsson, T., Raines, J. M., Slavin, J. A., Kullen, A., Sundberg, T., & Zurbuchen, T. H. (2015). Messenger observations of the dayside low-latitude boundary layer in mercury's magnetosphere. *Journal of Geophysical Research: Space Physics*, *120*(10), 8387–8400. https://doi.org/10.1002/2015JA021662

Liljeblad, E., Sundberg, T., Karlsson, T., & Kullen, A. (2014). Statistical investigation of Kelvin-Helmholtz waves at the magnetopause of Mercury. *Journal of Geophysical Research*, *119*(12), 9670–9683. https://doi.org/10.1002/2014JA020614

Murakami, G., Hayakawa, H., Ogawa, H., Matsuda, S., Seki, T., Kasaba, Y., et al. (2020). Mio—First comprehensive exploration of mercury's space environment: Mission overview. *Space Science Reviews*, *216*(7), 113. https://doi.org/10.1007/s11214-020-00733-3

Orsini, S., Milillo, A., Lichtenegger, H., Varsani, A., Barabash, S., Livi, S., et al. (2022). Inner southern magnetosphere observation of mercury via Serena ion sensors in bepicolombo mission. *Nature Communications*, *13*(1), 7390. https://doi.org/10.1038/s41467-022-34988-x

Raines, J. M., Dewey, R. M., Staudacher, N. M., Tracy, P. J., Bert, C. M., Sarantos, M., et al. (2022). Proton precipitation in mercury's northern magnetospheric cusp. *Journal of Geophysical Research: Space Physics*, *127*(11), e2022JA030397. https://doi.org/10.1029/2022JA030397

Raines, J. M., DiBraccio, G. A., Cassidy, T. A., Delcourt, D. C., Fujimoto, M., Jia, X., et al. (2015). Plasma sources in planetary magnetospheres: Mercury. *Space Science Reviews*, *192*(1), 91–144. https://doi.org/10.1007/s11214-015-0193-4

Raines, J. M., Gershman, D. J., Slavin, J. A., Zurbuchen, T. H., Korth, H., Anderson, B. J., & Solomon, S. C. (2014). Structure and dynamics of mercury's magnetospheric cusp: MESSENGER measurements of protons and planetary ions. *Journal of Geophysical Research*, *119*(8), 6587–6602. https://doi.org/10.1002/2014JA020120

Raines, J. M., Gershman, D. J., Zurbuchen, T. H., Sarantos, M., Slavin, J. A., Gilbert, J. A., et al. (2013). Distribution and compositional variations of plasma ions in mercury's space environment: The first three mercury years of messenger observations. *Journal of Geophysical Research*, *118*(4), 1604–1619. https://doi.org/10.1029/2012JA018073

Rojo, M., André, N., Aizawa, S., Sauvaud, J.-A., Saito, Y., Harada, Y., et al. (2024). Structure and dynamics of the herman magnetosphere revealed by electron observations from the mercury electron analyzer after the first three mercury flybys of bepicolombo. *A&A*, *687*, A243. https://doi.org/10.1051/0004-6361/202449450

Saito, Y., Delcourt, D., Hirahara, M., Barabash, S., André, N., Takashima, T., et al. (2021). Pre-flight calibration and near-earth commissioning results of the mercury plasma particle experiment (MPPE) onboard mmo (Mio). *Space Science Reviews*, *217*(5), 70. https://doi.org/10.1007/s11214-021-00839-2

Seki, K., Hirahara, M., Hoshino, M., Terasawa, T., Elphic, R., Saito, Y., et al. (2003). Cold ions in the hot plasma sheet of Earth's magnetotail. *Nature*, *422*(6932), 589–592. https://doi.org/10.1038/nature01502

Seki, K., Nagy, A., Jackman, C., Crary, F., Fontaine, D., Zarka, P., et al. (2015). A review of general physical and chemical processes related to plasma sources and losses for solar system magnetospheres. *Space Science Reviews*, *192*(1–4), 27–89. https://doi.org/10.1007/s11214-015-0170-y

Shabansky, V. P. (1971). Some processes in the magnetosphere. *Space Science Reviews*, *12*(3), 299–418. https://doi.org/10.1007/BF00165511

Shi, Z., Rong, Z. J., Fatemi, S., Slavin, J. A., Klinger, L., Dong, C., et al. (2022). An eastward current encircling mercury. *Geophysical Research Letters*, *49*(10), e2022GL098415. https://doi.org/10.1029/2022GL098415

Slavin, J. A. (2004). Mercury's magnetosphere. *Advances in Space Research*, *33*(11), 1859–1874. https://doi.org/10.1016/j.asr.2003.02.019

Slavin, J. A., Acuña, M. H., Anderson, B. J., Baker, D. N., Benna, M., Gloeckler, G., et al. (2008). Mercury's magnetosphere after MESSENGER's first flyby. *Science*, *321*(5885), 85–89. https://doi.org/10.1126/science.1159040

Slavin, J. A., Krimigis, S. M., Acuña, M. H., Anderson, B. J., Baker, D. N., Koehn, P. L., et al. (2007). Messenger: Exploring mercury's magnetosphere. In D. L. Domingue & C. T. Russell (Eds.), *The messenger mission to mercury* (pp. 133–160). Springer New York. https://doi.org/10.1007/978-0-387-77214-1_5

Sun, W., Dewey, R. M., Aizawa, S., Huang, J., Slavin, J. A., Fu, S., et al. (2022a). Review of mercury's dynamic magnetosphere: Post-messenger era and comparative magnetospheres. *Science China Earth Sciences*, *65*(1), 25–74. https://doi.org/10.1007/s11430-021-9828-0

Sun, W., Slavin, J. A., Milillo, A., Dewey, R. M., Orsini, S., Jia, X., et al. (2022b). Messenger observations of planetary ion enhancements at mercury's northern magnetospheric cusp during flux transfer event showers. *Journal of Geophysical Research: Space Physics*, *127*(4), e2022JA030280. https://doi.org/10.1029/2022JA030280

Sundberg, T., Boardsen, S., Slavin, J., Blomberg, L., & Korth, H. (2010). The kelvin–Helmholtz instability at mercury: An assessment. *Planetary and Space Science*, *58*(11), 1434–1441. https://doi.org/10.1016/j.pss.2010.06.008

Sundberg, T., Boardsen, S. A., Slavin, J. A., Anderson, B. J., Korth, H., Zurbuchen, T. H., et al. (2012). MESSENGER orbital observations of large-amplitude Kelvin-Helmholtz waves at Mercury's magnetopause. *Journal of Geophysical Research*, *117*(A4), A04216. https://doi.org/10.1029/2011JA017268

Sundberg, T., Boardsen, S. A., Slavin, J. A., Blomberg, L. G., Cumnock, J. A., Solomon, S. C., et al. (2011). Reconstruction of propagating kelvin–Helmholtz vortices at mercury's magnetopause. *Planetary and Space Science*, *59*(15), 2051–2057. https://doi.org/10.1016/j.pss.2011.05.008

Volland, H. (1978). A model of the magnetospheric electric convection field. *Journal of Geophysical Research*, *83*(A6), 2695–2699. https://doi.org/10.1029/JA083iA06p02695

Walsh, B. M., Ryou, A. S., Sibeck, D. G., & Alexeev, I. I. (2013). Energetic particle dynamics in mercury's magnetosphere. *Journal of Geophysical Research: Space Physics*, *118*(5), 1992–1999. https://doi.org/10.1002/jgra.50266

Winslow, R. M., Johnson, C. L., Anderson, B. J., Gershman, D. J., Raines, J. M., Lillis, R. J., et al. (2014). Mercury's surface magnetic field determined from proton-reflection magnetometry. *Geophysical Research Letters*, *41*(13), 4463–4470. https://doi.org/10.1002/2014GL060258

Winslow, R. M., Lugaz, N., Philpott, L., Farrugia, C. J., Johnson, C. L., Anderson, B. J., et al. (2020). Observations of extreme ICME ram pressure compressing mercury's dayside magnetosphere to the surface. *The Astrophysical Journal*, *889*(2), 184. https://doi.org/10.3847/1538-4357/ab6170

Zhao, J.-T., Zong, Q.-G., Slavin, J. A., Sun, W.-J., Zhou, X.-Z., Yue, C., et al. (2020). Proton properties in mercury's magnetotail: A statistical study. *Geophysical Research Letters*, *47*(19), e2020GL088075. https://doi.org/10.1029/2020GL088075

Zhao, J. T., Zong, Q. G., Yue, C., Sun, W. J., Zhang, H., Zhou, X. Z., et al. (2022). Observational evidence of ring current in the magnetosphere of mercury. *Nature Communications*, *13*(1), 924. https://doi.org/10.1038/s41467-022-28521-3

Zhong, J., Xie, L., Lee, L.-C., Slavin, J. A., Raines, J. M., Dewey, R. M., et al. (2024). North–south plasma asymmetry across mercury's near-tail current sheet. *Geophysical Research Letters*, *51*(1), e2023GL106266. https://doi.org/10.1029/2023GL106266

Zurbuchen, T. H., Raines, J. M., Gloeckler, G., Krimigis, S. M., Slavin, J. A., Koehn, P. L., et al. (2008). MESSENGER observations of the composition of mercury's ionized exosphere and plasma environment. *Science*, *321*(5885), 90–92. https://doi.org/10.1126/science.1159314

Zurbuchen, T. H., Raines, J. M., Slavin, J. A., Gershman, D. J., Gilbert, J. A., Gloeckler, G., et al. (2011). MESSENGER observations of the spatial distribution of planetary ions near mercury. *Science*, *333*(6051), 1862–1865. https://doi.org/10.1126/science.1211302